

# Multiplexed phase-space imaging for 3D fluorescence microscopy

HSIOU-YUAN LIU, JINGSHAN ZHONG AND LAURA WALLER

*Department of Electrical Engineering and Computer Sciences, University of California, Berkeley, USA*  
 hyluu@eecs.berkeley.edu, waller@eecs.berkeley.edu

**Abstract:** Phase-space, which is directly related to spatial coherence, describes spatial and angular information about a wave-field (e.g. light fields in ray optics). Phase-space measurements enable digital refocusing, aberration removal and 3D reconstruction. High-resolution capture of 4D phase-space datasets is, however, challenging. Scanning approaches are slow, light inefficient and have low resolution. Here, we propose a multiplexed method that solves these problems. We use a spatial light modulator (SLM) in the Fourier (pupil) plane of a microscope to pattern multiplexed coded apertures. Then, an inverse problem is solved based on regularized least squares with a proximal accelerated gradient descent solver. We experimentally image a  $670\ \mu\text{m} \times 259\ \mu\text{m} \times 500\ \mu\text{m}$  fluorescent sample in 3D with NA 0.4, demonstrating improved acquisition time, light throughput and resolution compared to a scanning aperture method. Data capture requirements are further reduced by regularization methods that exploit sparsity.

© 2022 Optical Society of America

**OCIS codes:** (100.3010) Image reconstruction techniques, (110.0180) Microscopy, (110.4980) Partial coherence in imaging, (110.1758) Computational imaging

## References and links

1. I. Cox, C. J. Sheppard, and T. Wilson, "Super-resolution by confocal fluorescent microscopy," *Optik* **60**, 391–396 (1982).
2. F. Helmchen and W. Denk, "Deep tissue two-photon microscopy," *Nature methods* **2**, 932–940 (2005).
3. T. A. Planchon, L. Gao, D. E. Milkie, M. W. Davidson, J. A. Galbraith, C. G. Galbraith, and E. Betzig, "Rapid three-dimensional isotropic imaging of living cells using Bessel beam plane illumination," *Nature methods* **8**, 417–423 (2011).
4. M. Levoy, R. Ng, A. Adams, M. Footer, and M. Horowitz, "Light field microscopy," in "SIGGRAPH '06," (New York, NY, USA, 2006), pp. 924–934.
5. M. Broxton, L. Grosenick, S. Yang, N. Cohen, A. Andalman, K. Deisseroth, and M. Levoy, "Wave optics theory and 3-d deconvolution for the light field microscope," *Optics express* **21**, 25418–25439 (2013).
6. S. R. P. Pavani, M. A. Thompson, J. S. Biteen, S. J. Lord, N. Liu, R. J. Twieg, R. Piestun, and W. Moerner, "Three-dimensional, single-molecule fluorescence imaging beyond the diffraction limit by using a double-helix point spread function," *Proceedings of the National Academy of Sciences* **106**, 2995–2999 (2009).
7. Y. Shechtman, L. E. Weiss, A. S. Backer, S. J. Sahl, and W. E. Moerner, "Precise three-dimensional scan-free multiple-particle tracking over large axial ranges with tetrapod point spread functions," *Nano Letters* **15**, 4194–4199 (2015). PMID: 25939423.
8. M. Testorf, B. Hennelly, and J. Ojeda-Castañeda, *Phase-Space Optics: Fundamentals and Applications* (McGraw-Hill Professional, 2009).
9. M. Bastiaans, "The Wigner distribution function applied to optical signals and systems," *Opt. Commun.* **25**, 26 – 30 (1978).
10. A. Accardi and G. Wornell, "Quasi light fields: extending the light field to coherent radiation," *J. Opt. Soc. Am. A* **26**, 2055–2066 (2009).
11. Z. Zhang and M. Levoy, "Wigner distributions and how they relate to the light field," in "Computational Photography (ICCP), 2009 IEEE International Conference on," (2009), pp. 1–10.
12. R. Ng, M. Levoy, M. Bredif, G. Duval, M. Horowitz, and P. Hanrahan, "Light field photography with a hand-held plenoptic camera," *Tech. Rep. CTSR 2005-02*, Stanford (2005).
13. R. Ng, "Digital light field photography," Ph.D. thesis, Stanford, CA, USA (2006). AAI3219345.
14. R. Ng and P. Hanrahan, "Digital correction of lens aberrations in light field photography," in "Contract Proceedings 2006," (International Society for Optics and Photonics, 2007), pp. 63421E–63421E.
15. D. Christodoulides, E. Eugenieva, T. Coskun, M. Segev, and M. Mitchell, "Equivalence of three approaches describing partially incoherent wave propagation in inertial nonlinear media," *Phys. Rev. E* **63**, 35601 (2001).
16. D. L. Marks, R. A. Stack, and D. J. Brady, "Three-dimensional coherence imaging in the Fresnel domain," *Appl. Opt.* **38**, 1332–1342 (1999).

17. H.-Y. Liu, E. Jonas, L. Tian, J. Zhong, B. Recht, and L. Waller, "3D imaging in volumetric scattering media using phase-space measurements," *Opt. Express* **23**, 14461–14471 (2015).
18. L. Waller, L. Tian, G. Barbastathis, and J. W. Fleischer, "Wave-field imaging with partially coherent light," in "Applied Industrial Optics: Spectroscopy, Imaging and Metrology," (Optical Society of America, 2012), pp. AW3B–3.
19. H.-Y. Liu, L. Tian, and L. Waller, "High-speed and high-resolution phase-space imaging with digital micromirror devices," in "Imaging and Applied Optics 2014," (Optical Society of America, 2014), p. JW3A.1.
20. C.-K. Liang, T.-H. Lin, B.-Y. Wong, C. Liu, and H. H. Chen, "Programmable aperture photography: Multiplexed light field acquisition," in "ACM SIGGRAPH 2008 Papers," (ACM, New York, NY, USA, 2008), SIGGRAPH '08, pp. 55:1–55:10.
21. P. Green, W. Sun, W. Matusik, and F. Durand, "Multi-aperture photography," in "ACM Transactions on Graphics (TOG)," , vol. 26 (ACM, 2007), vol. 26, p. 68.
22. C. Zhou and S. Nayar, "What are good apertures for defocus deblurring?" in "Computational Photography (ICCP), 2009 IEEE International Conference on," (IEEE, 2009), pp. 1–8.
23. Y. Y. Schechner, R. Piestun, and J. Shamir, "Wave propagation with rotating intensity distributions," *Phys. Rev. E* **54**, R50–R53 (1996).
24. Y. Shechtman, S. J. Sahl, A. S. Backer, and W. E. Moerner, "Optimal point spread function design for 3d imaging," *Phys. Rev. Lett.* **113**, 133902 (2014).
25. N. Ji, D. E. Milkie, and E. Betzig, "Adaptive optics via pupil segmentation for high-resolution imaging in biological tissues," *Nature Methods* **7**, 141–147 (2010).
26. A. Beck and M. Teboulle, "A fast iterative shrinkage-thresholding algorithm for linear inverse problems," *SIAM Journal on Imaging Sciences* **2**, 183–202 (2009).
27. A. V. Gitin and M. P. Kalashnikov, "Hyperbolic rotation of the wigner distribution function," *Appl. Opt.* **54**, D8–D14 (2015).
28. M. J. Bastiaans, "Application of the Wigner distribution function to partially coherent light," *J. Opt. Soc. Am. A* **3**, 1227–1238 (1986).
29. J. Goodman, *Introduction to Fourier optics* (Roberts & Co., 2005).
30. M. Bertero and P. Boccacci, "A simple method for the reduction of boundary effects in the Richardson-Lucy approach to image deconvolution," *Astronomy and Astrophysics* **437**, 369–374 (2005).

## 1. Introduction

3D fluorescence microscopy is a critical tool in biological microscopy, since most samples are thick and can be functionally labeled. For high-resolution 3D imaging, the main methods used are confocal microscopy [1], two-photon [2] and light sheet imaging [3]. Because these methods all involve scanning, they are inherently limited in terms of speed or volume. Light field microscopy [4, 5], on the other hand, achieves single-shot 3D capture at a cost of severe resolution loss. Single-shot coded aperture imaging [6, 7] can reconstruct 3D fluorescent scenes with good resolution, if the sample is extremely sparse. Here, we seek a multi-shot method that uses efficient and flexible data capture to reconstruct large dense volumes with high resolution.

Our work fits into the framework of phase-space optics, which is the general term for any space-angle description of light [8–11]. Light fields, for example, are phase-space functions for ray optics with incoherent light. The light field describes each ray's position and angle at a particular plane. Light field measurements have been used for digital refocusing [12, 13], aberration removal [14] and 3D reconstruction. In microscopy, wave-optical effects become prominent and so ray optics no longer suffices. Hence, we switch to using Wigner functions, which are the wave-optical analog to light fields [11].

The Wigner function describes spatial and spatial frequency (propagation angle) information for a wave-field of arbitrary coherence; it converges to the light field in the limit of incoherent ray optics [11]. Wigner functions contain the same information as as the mutual intensity function or a coherent mode decomposition; each of which can be derived as a unitary mathematical transform of the Wigner function [8, 15]. In the case of fluorescence microscopy, where the object is a set of incoherent emitters, the Wigner function represents the incoherent 3D Optical Transfer Function (OTF) [8]. As a type of spatial coherence imaging [16], Wigner measurement can be used for 3D reconstructions in scattering media [17].

Phase-space imaging is 4D, with two spatial and two spatial-frequency coordinates. This high dimensionality poses measurement challenges [18, 19]. In single-shot schemes, the 2D sensor

pixels must be distributed across 4D, severely restricting resolution. Our experimental setup consists of a spatial light modulator (SLM) in Fourier space to implement aperture patterns, while collecting multiple 2D intensity images in real space (Fig. 1). In previous work [19], the SLM scanned a small aperture through Fourier space, capturing 2D intensity images for each spatial frequency. The acquired 4D phase space thus has very large pixel count - the product of the pixel counts of the SLM and the sensor (typically  $\sim 10^{12}$ ). These large datasets present challenges for data storage, and acquisition is slow ( $\sim 10$  minutes), limiting applications. We seek here a flexible trade-off between time and resolution, with ability to exploit sparsity for further data reduction, by using a multiplexed measurement approach.

In this work, the SLM implements a series of quasi-random coded aperture patterns (the optimal patterns are object-dependent). Compared to the scanning aperture method [18, 19], the new scheme has three major benefits. First, it achieves better resolution by capturing high-frequency interference effects (high-order correlations). This enables diffraction-limited resolution that is set by the microscope's NA, rather than by the scanned aperture. Second, we achieve higher light throughput by opening up more of the pupil; this can be traded for shorter exposure time and faster acquisition. Finally, the multiplexed nature of the measurements enables application of compressed-sensing ideas that exploit sparsity to capture fewer images for a given 4D resolution.

Our method can be alternately described as diffraction-limited 3D fluorescence microscopy with multiple coded apertures, similar to computational photography [20–22] and microscopy [6, 23–25]. In our case, we use a wave-optical model to fully account for diffraction effects, so intensity measurements are nonlinear with complex-field. However, the mutual incoherence of different fluorophores allows a simplification on the forward model. We model each fluorophore as a single coherent mode - it is coherent with itself but incoherent with all other fluorophores. Our reconstruction algorithm is a large-scale inverse problem akin to multi-image 3D deconvolution, formulated as a convex  $\ell_1$  regularized least-square error problem and solved by a fast iterative shrinkage-thresholding algorithm (FISTA) [26].

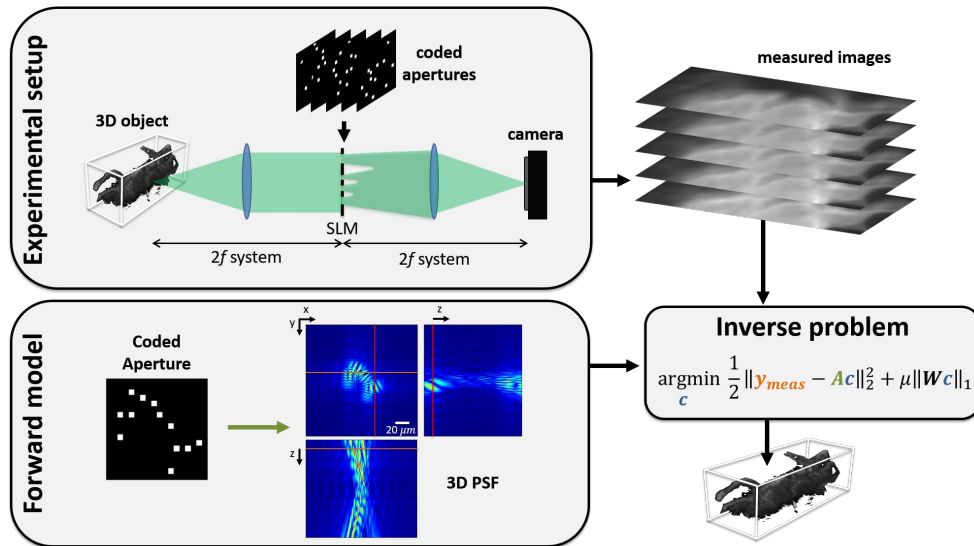


Fig. 1. Phase-space multiplexing for 3D fluorescence microscopy. The microscope (a  $4f$  system) uses a Spatial Light Modulator (SLM) in Fourier space to implement multiple coded apertures, while capturing 2D intensity images in real space for each. Our wave-optical forward model (A) relates the sample ( $c$ ) to the measured images ( $y_{meas}$ ) for each pattern. The inverse problem recovers the sample, possibly subject to sparsity priors.

## 2. Theory and methods

In this section we use the Wigner function (WF) and its close relative Mutual Intensity (MI) to describe the multiplexing process, then specify our scheme for 3D fluorescent microscopy. The WF is a function of position and spatial frequency, where spatial frequency can be thought of as the direction of ray propagation in geometrical optics. Here we assume the light is quasi-monochromatic, temporally stationary and ergodic [8, 9, 27, 28]. The Wigner function is:

$$W(\mathbf{u}, \mathbf{r}) \triangleq \iint \left\langle \tilde{E}^*\left(\mathbf{u} - \frac{\Delta\mathbf{u}}{2}\right) \tilde{E}\left(\mathbf{u} + \frac{\Delta\mathbf{u}}{2}\right) \right\rangle e^{i2\pi(\Delta\mathbf{u}) \cdot \mathbf{r}} d^2(\Delta\mathbf{u}), \quad (1)$$

where  $\mathbf{r} = (x, y)$  denotes transverse spatial coordinates,  $\mathbf{u} = (u_x, u_y)$  denotes spatial frequency coordinates and  $\langle \cdot \rangle$  denotes ensemble average. The quantity contained by angle brackets

$$\text{MI}(\mathbf{u}, \Delta\mathbf{u}) \triangleq \left\langle \tilde{E}^*\left(\mathbf{u} - \frac{\Delta\mathbf{u}}{2}\right) \tilde{E}\left(\mathbf{u} + \frac{\Delta\mathbf{u}}{2}\right) \right\rangle \quad (2)$$

is, apart from a coordinate transform, the Mutual Intensity.  $E(\mathbf{r})$  is a coherent mode of the electric field (e.g. a fluorophore) and  $\tilde{E}(\mathbf{u})$  is its Fourier transform. The ensemble average enables representation of both coherent and partially spatially coherent light, with multiple wavelengths being accounted for by integrating the WFs for each. Here, we assume that the sample is a 3D volume of incoherent emitters with no occlusions. Thus, the phase-space description of light from the sample is a linear sum of that from each fluorophore.

The aperture patterns are applied in the pupil plane (see Fig. 1) while intensity images are captured in real space. Based on the raw data and forward model, the reconstruction problem is formulated as a nonlinear optimization procedure. When the sample does not fill the entire 3D volume, we use a sparsity prior to reduce the number of images necessary for full phase-space capture. In previous work [17], we accounted for scattering (e.g. in biological tissue) by incorporating a scattering model into the forward problem. For simplicity, we assume here no scattering, though incorporating the model is straightforward.

### 2.1. Forward model

Our forward model relates the captured images to the 3D object, for each multiplexed pattern. Each image contains information from multiple frequencies and their interference terms (which are key to resolution enhancement). The MI framework facilitates our mathematical analysis. The operation of applying the 3D Optical Transfer Function (OTF) to an incoherent source is equivalent to projecting a mask in MI space (see Fig. 2). MI analysis can further reveal interference effects that may be obscured by looking only at this projected quantity, aiding in mask design. For simplicity, we first describe the forward model of a single coherent mode (e.g. a single point source) and then generalize to multiple modes.

A coherent mode,  $E_s(\mathbf{r}_1; \alpha)$ , is a complex electric field that interferes coherently with itself but not with other modes. Each point source in a scene may constitute a unique coherent mode, specified by the properties of the source,  $\alpha$  (e.g. location, wavelength). Consider a single coherent mode on the front focal plane of the  $4f$  system in Fig. 1. The complex-field just before the SLM can be described by the Fourier transform of the complex field [29], expressed as  $\tilde{E}_s(\mathbf{u}_1, \alpha)$ , where  $\mathbf{u}_1$  is in units of spatial frequency that relate to the lateral coordinates  $\mathbf{x}_1$  on the SLM by multiplying the wavelength  $\lambda$  and the front focal length  $f$ , such that  $\mathbf{x}_1 = \lambda f \mathbf{u}_1$ . The field  $\tilde{E}_s(\mathbf{u}_1; \alpha)$  is then multiplied by the aperture pattern on the SLM, giving

$$\tilde{E}_n(\mathbf{u}_1; \alpha) = M_n(\lambda f \mathbf{u}_1) \tilde{E}_s(\mathbf{u}_1; \alpha), \quad (3)$$

where  $\tilde{E}_n$  is the patterned complex-field in Fourier space and  $M_n$  represents the  $n$ 'th binary SLM

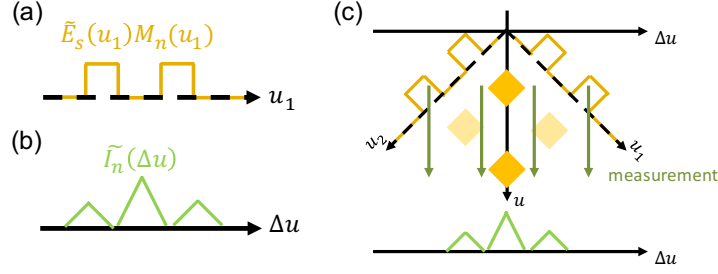


Fig. 2. Illustration of how a 1D complex-field is patterned in Mutual Intensity (MI) space by a particular coded aperture pattern. The resulting intensity is a projection in the MI domain after patterning by the aperture. (a) In Fourier space, the complex-field is multiplied by an aperture pattern  $M_n$ , here consisting of two open holes. (b) The corresponding intensity image at the sensor is related through (c) MI domain. If  $\tilde{E}_s M_n$  is defocused, the intensity projections define the 3D OTF of the system. In this example, the  $\tilde{E}_s M_n$  captures MI information from 4 diamond-shaped areas, which is preferable to the aperture scanning case (not shown) which contains only one such diamond on the  $u$ -axis. The information gained by capturing the light yellow diamonds provides diffraction-limited resolution.

pattern. At the sensor plane (the back focal plane of the  $4f$  system) the intensity  $I_n$  is:

$$I_n(\mathbf{r}; \alpha) = \iint \tilde{E}_n(\mathbf{u}_1; \alpha) e^{i2\pi\mathbf{u}_1 \cdot \mathbf{r}} d^2\mathbf{u}_1 \iint \tilde{E}_n^*(\mathbf{u}_2; \alpha) e^{-i2\pi\mathbf{u}_2 \cdot \mathbf{r}} d^2\mathbf{u}_2, \quad (4)$$

where  $\mathbf{u}_2$  is a duplicate of  $\mathbf{u}_1$ . The intensity image can be alternately related to the MI or WF by a simple coordinate transform  $\mathbf{u}_1 = \mathbf{u} + \Delta\mathbf{u}/2$ ,  $\mathbf{u}_2 = \mathbf{u} - \Delta\mathbf{u}/2$ :

$$I_n(\mathbf{r}; \alpha) = \iiint \tilde{E}_n(\mathbf{u} + \Delta\mathbf{u}/2; \alpha) \tilde{E}_n^*(\mathbf{u} - \Delta\mathbf{u}/2; \alpha) e^{i2\pi\Delta\mathbf{u} \cdot \mathbf{r}} d^2\Delta\mathbf{u} d^2\mathbf{u} \quad (5)$$

$$= \iiint \text{MI}_n(\mathbf{u}, \Delta\mathbf{u}; \alpha) e^{i2\pi\Delta\mathbf{u} \cdot \mathbf{r}} d^2\Delta\mathbf{u} d^2\mathbf{u} \quad (6)$$

$$= \iint W_n(\mathbf{u}, \mathbf{r}; \alpha) d^2\mathbf{u}, \quad (7)$$

where  $\text{MI}_n$  and  $W_n$  are the MI and WF associated with the field modified by the  $n$ 'th mask.

Visualizing the intensity measurement in terms of both its WF and MI gives new insights. Eq. (7) shows that the intensity image is a projection of the patterned phase space  $W_n$ . Alternately, looking at the Fourier transform of  $I_n$ , denoted by  $\tilde{I}_n$ , we can interpret the intensity measurement as a patterning and projection of the source MI:

$$\begin{aligned} \tilde{I}_n(\Delta\mathbf{u}; \alpha) &= \iint \text{MI}_n(\mathbf{u}, \Delta\mathbf{u}; \alpha) d^2\mathbf{u} \\ &= \iint M_n^* \left( \lambda f \left( \mathbf{u} - \frac{\Delta\mathbf{u}}{2} \right) \right) M_n \left( \lambda f \left( \mathbf{u} + \frac{\Delta\mathbf{u}}{2} \right) \right) \text{MI}_s(\mathbf{u}, \Delta\mathbf{u}; \alpha) d^2\mathbf{u}, \end{aligned} \quad (8)$$

where  $\text{MI}_s$  is the MI of source field  $E_s$ . This interpretation is illustrated for a 1D complex-field in Fig. 2. Each SLM pattern probes different parts of the source MI, which we wish to reconstruct. One can use this framework to help design optimal coded aperture patterns.

The extension of our forward model to multiple coherent modes is straightforward. Since each mode is mutually incoherent with others, we simply sum over all of them with their own weights  $c(\alpha)$ . The resulting formula, with  $I_n(\mathbf{r}; \alpha)$  given in Eqs. (6) and (8), is:

$$I_n(\mathbf{r}) = \sum_{\alpha} c(\alpha) I_n(\mathbf{r}; \alpha). \quad (9)$$

## 2.2. Applying multiplexed measurements to fluorophores

We specify  $\tilde{E}_s$  in Eq. (3) to be from a finite-bandwidth fluorophore located at position  $(\mathbf{r}_s, z_s)$  where  $z_s$  is the defocus distance from the front focal plane of the  $4f$  system in Fig. 1. The parameter  $\alpha$  is  $(\mathbf{r}_s, z_s, \lambda)$  for a single mode, and our goal is to solve for the strength of each via coefficients  $c(\alpha)$ . To account for off-focus point sources, the field can be propagated to  $-z_s$ :

$$\tilde{E}_s(\mathbf{u}_1; \mathbf{r}_s, z_s, \lambda) = \begin{cases} e^{i \frac{2\pi}{\lambda} (-z_s) \sqrt{1-\lambda^2} |\mathbf{u}_1|^2 - i 2\pi \mathbf{r}_s \cdot \mathbf{u}_1}, & |\mathbf{u}_1| < \frac{NA}{\lambda} \\ 0, & \text{otherwise} \end{cases}, \quad (10)$$

where  $NA$  is the numerical aperture of the  $4f$  system,  $\lambda$  is wavelength of a mode and we use angular spectrum propagation [29]. Using Eqs. (2), (6), (8) and some algebra, intensity becomes

$$I_n(\mathbf{r}; \mathbf{r}_s, z_s, \lambda) = \iint K_{M_n, z_s}(\Delta \mathbf{u}; \lambda) e^{i 2\pi (\mathbf{r} - \mathbf{r}_s) \cdot \Delta \mathbf{u}} d^2 \Delta \mathbf{u}, \quad (11)$$

where

$$K_{M_n, z_s}(\Delta \mathbf{u}; \lambda) = \iint M_n^* \left( \lambda f \left( \mathbf{u} - \frac{\Delta \mathbf{u}}{2} \right) \right) M_n \left( \lambda f \left( \mathbf{u} + \frac{\Delta \mathbf{u}}{2} \right) \right) e^{i \frac{2\pi z_s}{\lambda} \left( \sqrt{1-\lambda^2} \left| \mathbf{u} - \frac{\Delta \mathbf{u}}{2} \right|^2 - \sqrt{1-\lambda^2} \left| \mathbf{u} + \frac{\Delta \mathbf{u}}{2} \right|^2 \right)} d^2 \mathbf{u} \quad (12)$$

is a kernel for mask  $M_n$  and depth  $z_s$ . Plugging Eq. (11) into Eq. (9) gives the final expression of the forward model. Before doing so, we assume the fluorescent spectrum is identical for all fluorophores and decompose  $c(\alpha)$  into a product of the spectral weight and 3D distribution of fluorophores,  $c(\alpha) = S(\lambda)C(\mathbf{r}_s, z_s)$ . With this we have the final expression following Eq. (9),

$$I_n(\mathbf{r}) = \iiint \left( \iint \sum_{\lambda} S(\lambda) K_{M_n, z_s}(\Delta \mathbf{u}; \lambda) e^{i 2\pi (\mathbf{r} - \mathbf{r}_s) \cdot \Delta \mathbf{u}} d^2 \Delta \mathbf{u} \right) C(\mathbf{r}_s, z_s) d^2 \mathbf{r}_s dz_s. \quad (13)$$

Equation (13) describes the forward model for the intensity images with an input 3D fluorophore distribution  $C(\mathbf{r}_s, z_s)$ . Here the spectral weights  $S(\lambda)$  can be measured directly (or may be known a priori). The term in the parenthesis is a convolution kernel which can be interpreted (as in Fig. 1) as a 3D point spread function (PSF) for mask  $M_n$ .

## 2.3. Inverse problem

Our goal is to reconstruct the 3D fluorescence distribution  $C(\mathbf{r}_s, z_s)$  from the measured intensity images. We formulate the inverse problem as a minimization of data mismatch with a regularizer. The mismatch is defined as the least-square error between the measured intensity images and the intensity predicted by our forward model (Eq. (13)). We use an  $\ell_1$  regularizer to mitigate the effects of noise. This formulation has a smooth part and a non smooth part in the objective function and can be efficiently solved by a proximal gradient descent solver (e.g. FISTA [26]).

To formulate the inverse problem, we first discretize the forward model in Eq. (13) to be

$$\mathbf{y} = \mathbf{A} \mathbf{c}. \quad (14)$$

Here  $\mathbf{y} \in \mathbb{R}^{M \times P \times 1}$  corresponds to predicted images on the sensor, each small chunk ( $\in \mathbb{R}^{P \times 1}$ ) of which is a vectorized image  $I_n(\mathbf{r})$ .  $\mathbf{r}$  discretizes into  $P$  pixels and the number of masks is  $M$ , so  $n = 1 \dots M$ . Similarly, we discretize  $\mathbf{r}_s$  and  $z_s$  into  $P'$  and  $L$  samples, respectively, to obtain a vectorized version of  $C(\mathbf{r}_s, z_s)$  ( $\mathbf{c} \in \mathbb{R}^{L \times P' \times 1}$ ). The matrix  $\mathbf{A} \in \mathbb{R}^{M \times P \times L \times P'}$ , which is not materialized, carries out the summation and convolution in Eq. (13) using 2D Fast Fourier Transform (FFT) for each subvector ( $\in \mathbb{R}^{P' \times 1}$ ) of  $\mathbf{c}$ . The FFT uses zero-padding to avoid periodic boundary condition errors, and the convolution kernel is precomputed and stored for speed.

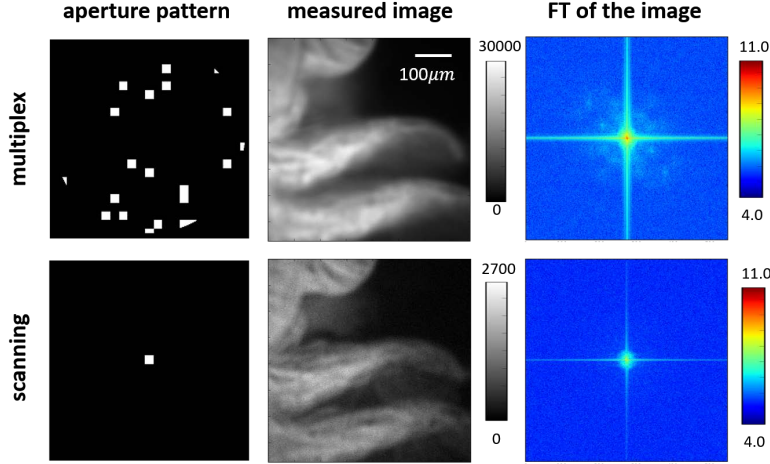


Fig. 3. Comparison between scanning aperture and multiplexed phase-space measurements. (Left) An example aperture pattern, (Middle) the corresponding measured intensity images (same exposure time; note that the multiplexed image has higher intensity values). (Right) log-scale Fourier transform of the measured images, demonstrating that the multiplexed measurements have more high-frequency content, giving better final resolution.

The inverse problem can then be expressed as:

$$\arg \min_{\mathbf{c} \geq 0} \frac{1}{2} \|\mathbf{y} - \mathbf{y}_{\text{meas}}\|_2^2 + \mu \|\mathbf{W}\mathbf{c}\|_1, \quad (15)$$

where  $\mathbf{y}_{\text{meas}} \in \mathbb{R}^{MP \times 1}$  is the measured intensity and  $\mu$  is the  $\ell_1$  regularization parameter. Here, we additionally use a diagonal matrix  $\mathbf{W} \in \mathbb{R}^{LP' \times LP'}$  to lower the weight for the point sources near the borders of images since some of their light falls off the sensor. Each diagonal entry of  $\mathbf{W}$  is obtained by summing the corresponding column in  $\mathbf{A}$ . There can also be outside point sources that contribute to the measured intensity due to defocus; hence, we use an extended field of view method [30] to solve for more sample points in  $\mathbf{c}$  than  $\mathbf{y}$  (*i.e.*  $P' > P$ ).

#### 2.4. Comparison between multiplexing and scanning aperture spectrograms

In the scanning-aperture scheme [18, 19], the aperture should be small to ensure good frequency sampling of the 4D function; however, smaller apertures result in 1) lower resolution, 2) lower signal-to-noise ratio (SNR) and 3) large data sets. Our multiplexing scheme alleviates all of these problems. Figure 3 addresses the first two concerns. Multiplexing enhances the diffraction-limited resolution of the final reconstruction by capturing more frequency content in each image. This is evident in the Fourier transform of the captured images, shown in Fig. 3. The SNR improvement of the multiplexing scheme is also visible in the measured images, with the multiplexed image being less noisy. Importantly, the number of multiplex patterns is flexible. For instance, by increasing the number of openings in a pattern, we can cover the entire pupil with fewer patterns. This means that we may be able to reconstruct the object from fewer measurements, if the inverse problem is solvable. By imposing constraints representing *a priori* information about the object (such as sparsity in 3D), we may solve the inverse problem with fewer total measured pixels than we have voxels in the reconstruction.

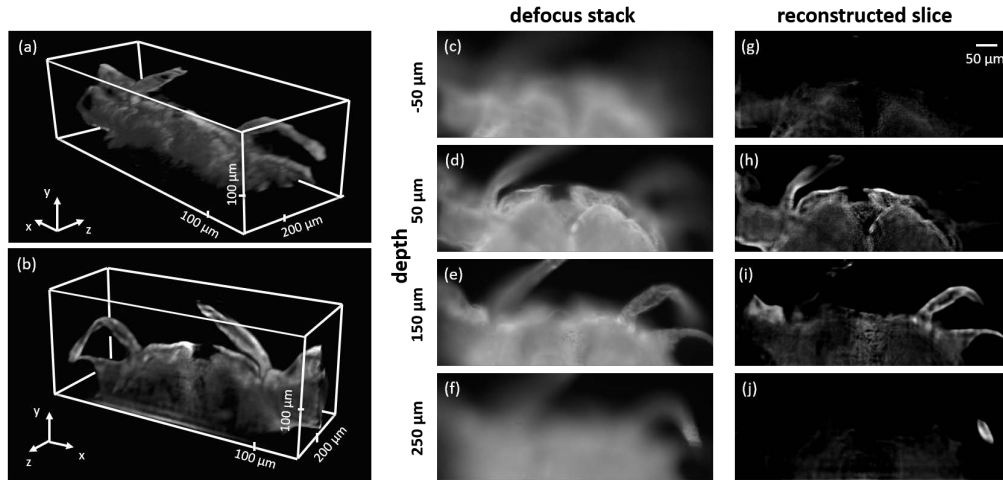


Fig. 4. Reconstruction of a brine shrimp fluorescent sample and comparison with through-focus intensity image stack. (a,b) 3D emission map rendering of the reconstructed fluorophores, viewed from different perspectives. The recovered 3D volume is  $670 \mu\text{m} \times 259 \mu\text{m} \times 500 \mu\text{m}$ . (c)-(f) Separately measured images at different focus planes for comparison. (g)-(j) slices of the reconstructed volume at each corresponding depth in (b)-(e).

### 2.5. Mask design

Our masks are chosen by quasi-random non-replacement selection. We section the SLM plane into  $23 \times 23$  square blocks and keep only the 429 blocks that are inside the system NA. For each mask, we open 20 blocks, selected randomly from the blocks remaining after excluding ones that were open in previous sequences. In this scheme, the full NA can be covered by 22 masks. To allow for some measurement redundancy, we choose to cover the entire pupil 4 times, resulting in 100 multiplexed aperture patterns, one of which is shown in Fig. 3.

## 3. Experiments

Our experimental setup is shown in Fig. 1. The lens collecting the light from the sample is a Nikon infinity-corrected objective with  $20\times$  magnification and NA 0.4. The back focal plane of the objective is inaccessible, so we use the objective and a tube lens  $f = 200 \text{ mm}$  to relay the image to the sample plane. The  $4f$  system in Fig. 1 is built upon the relayed image, with the first lens  $f = 250 \text{ mm}$  and the second one  $f = 225 \text{ mm}$ . The SLM, a  $1400 \times 1050$  pixel liquid crystal chip from a 3-LCOS projector (Canon SX50, pixel size  $10.3 \mu\text{m}$ ) is reflective and polarization-sensitive, so we fold the optical train with a polarization beam splitter and insert linear polarizers. The multiplexed patterns are sent to the SLM chip through the VGA port of the projector. We use a camera sensor (Hamamatsu ORCA-Flash4.0 V2) to capture the multiplexed images and synchronize with the SLM via computer control.

Our experiments use a fluorescent brine shrimp sample (Carolina Biological) that is large and dense. The result shown in Fig. 4(a,b) is stitched from three volume reconstructions, each with  $640 \times 640 \times 120$  voxels to represent the sample volume of  $461 \mu\text{m} \times 461 \mu\text{m} \times 600 \mu\text{m}$ . The reconstruction is cropped to the central part of our extended field of view. The final volume contains  $930 \times 360 \times 100$  voxels corresponding to  $670 \mu\text{m} \times 259 \mu\text{m} \times 500 \mu\text{m}$ . Our reconstruction has good optical depth sectioning; Fig. 4 (c) to (j) shows slices of the reconstruction at different depths having better rejection of information from other depths than traditional intensity images

captured through-focus in a focus stack. The resolution of the reconstructed slices is slightly lower than the defocus stack. This may be related to experimental errors, or the missing information in the frequency mutual intensity illustrated in Fig. 2(c) because our scheme greatly undersamples this MI (there are roughly  $429 \times 439/2 = 92020$  independent blocks in this 4D MI). The acquisition time is greatly reduced compared to aperture scanning, which would require 429 measurements, one for each block in Fourier space. Here, we use only 100 measurements, and obtain much higher light throughput for better SNR.

The large dataset size means that the time and computational resources required are significant. Since the size of the 3D array is  $\approx 5 \times 10^7$  without the extended field-of-view and the measured data is  $\approx 2 \times 10^7$ , the number of required floating number operations for evaluating Eq. (13) with FFT is on the order of  $3 \times 10^{10}$ . This takes 28 seconds to compute on a computer with 24-core 2.0 GHz CPUs. The memory required to store the kernel (Eq. (12)) is 146 GB.

#### **4. Conclusion**

We demonstrated 3D reconstruction of a large-volume high-resolution dense fluorescent sample with multiplexed phase-space measurements. An SLM in Fourier space dynamically patterns the aperture while multiple intensity images are collected in real space. Theory is developed in phase-space, with relation to Mutual Intensity functions and 3D OTFs. Reconstruction is formulated as an  $\ell_1$ -regularized least-square problem with sparsity priors. This method enables diffraction-limited imaging with high resolution across very large volumes, efficient data capture and fast acquisition that is flexible for different types and sizes of samples.

#### **Funding**

The Office of Naval Research (ONR) (N00014-14-1-0083).

#### **ACKNOWLEDGMENTS**

The authors thank Eric Jonas, Ben Recht and the AMP Lab at UC Berkeley for help with computational resources.